



# Role of climate and vegetation density in modulating denudation rates in the Himalaya



Stephanie M. Olen\*, Bodo Bookhagen, Manfred R. Strecker

*Institute of Earth and Environmental Science, University of Potsdam, 14476 Potsdam, Germany*

## ARTICLE INFO

### Article history:

Received 2 October 2015  
Received in revised form 29 March 2016  
Accepted 30 March 2016  
Available online xxxx  
Editor: A. Yin

### Keywords:

geomorphology  
erosion  
vegetation  
rainfall  
Himalaya  
10-Be terrestrial cosmogenic nuclides

## ABSTRACT

Vegetation has long been hypothesized to influence the nature and rates of surface processes. We test the possible impact of vegetation and climate on denudation rates at orogen scale by taking advantage of a pronounced along-strike gradient in rainfall and vegetation density in the Himalaya. We combine 12 new  $^{10}\text{Be}$  denudation rates from the Sutlej Valley and 123 published denudation rates from fluvially-dominated catchments in the Himalaya with remotely-sensed measures of vegetation density and rainfall metrics, and with tectonic and lithologic constraints. In addition, we perform topographic analyses to assess the contribution of vegetation and climate in modulating denudation rates along strike. We observe variations in denudation rates and the relationship between denudation and topography along strike that are most strongly controlled by local rainfall amount and vegetation density, and cannot be explained by along-strike differences in tectonics or lithology. A W–E along-strike decrease in denudation rate variability positively correlates with the seasonality of vegetation density ( $R = 0.95$ ,  $p < 0.05$ ), and negatively correlates with mean vegetation density ( $R = -0.84$ ,  $p < 0.05$ ). Vegetation density modulates the topographic response to changing denudation rates, such that the functional relationship between denudation rate and topographic steepness becomes increasingly linear as vegetation density increases. We suggest that while tectonic processes locally control the pattern of denudation rates across strike of the Himalaya (i.e., S–N), along strike of the orogen (i.e., E–W) climate exerts a measurable influence on how denudation rates scatter around long-term, tectonically-controlled erosion, and on the functional relationship between topography and denudation.

© 2016 Elsevier B.V. All rights reserved.

## 1. Introduction

The role of vegetation in shaping landscapes and moderating denudation has been long recognized (e.g., Langbein and Schumm, 1958), but our understanding of the influence of vegetation cover over differing time and spatial scales remains incomplete (e.g., Dietrich and Perron, 2006). Langbein and Schumm (1958) posited that as effective precipitation increases, sediment yield will increase until there is sufficient precipitation to support a stable vegetation cover, causing subsequent decrease in sediment yield. Modeling studies have suggested that vegetation inhibits erosion and ultimately creates steeper landscapes, resulting in more variable and extreme erosion events (e.g., landsliding) than in analogous environments with less or no vegetation (Collins et al., 2004; Istanbuluoglu et al., 2004; Istanbuluoglu and Bras, 2005). Several field studies have demonstrated that the absence of vegetation following wildfires or forest degradation leads to a significant in-

crease in erosion and sediment yield over short timescales (e.g., Lamb et al., 2011; West et al., 2015). However, the general applicability of these findings has not been confirmed in large-scale field studies, or over longer timescales. While some large-scale studies have addressed this problem in recent years (Carretier et al., 2013; Torres Acosta et al., 2015), documenting how vegetation influences denudation rates in active orogens can prove difficult due to the strong interdependence of tectonics, topography, regional climate, and vegetation.

In the Himalaya, the present-day climate is strongly influenced by tectonically-created topography. Seasonal rainfall from the Indian Summer Monsoon (ISM) is focused at orographic barriers along the southern flank of the orogen (Fig. 1A) (Bookhagen and Burbank, 2010), although this effect decreases toward the west. In general, vegetation density (Fig. 1B) is highly influenced by available moisture and temperature, which are controlled primarily by geographic location and elevation. Thus, across strike of the orogen, peak rainfall and vegetation density correspond to orographic barriers and coincide with abrupt increases in topographic steepness. The resulting high interdependence of climate, vegetation,

\* Corresponding author.

E-mail address: olen@geo.uni-potsdam.de (S.M. Olen).

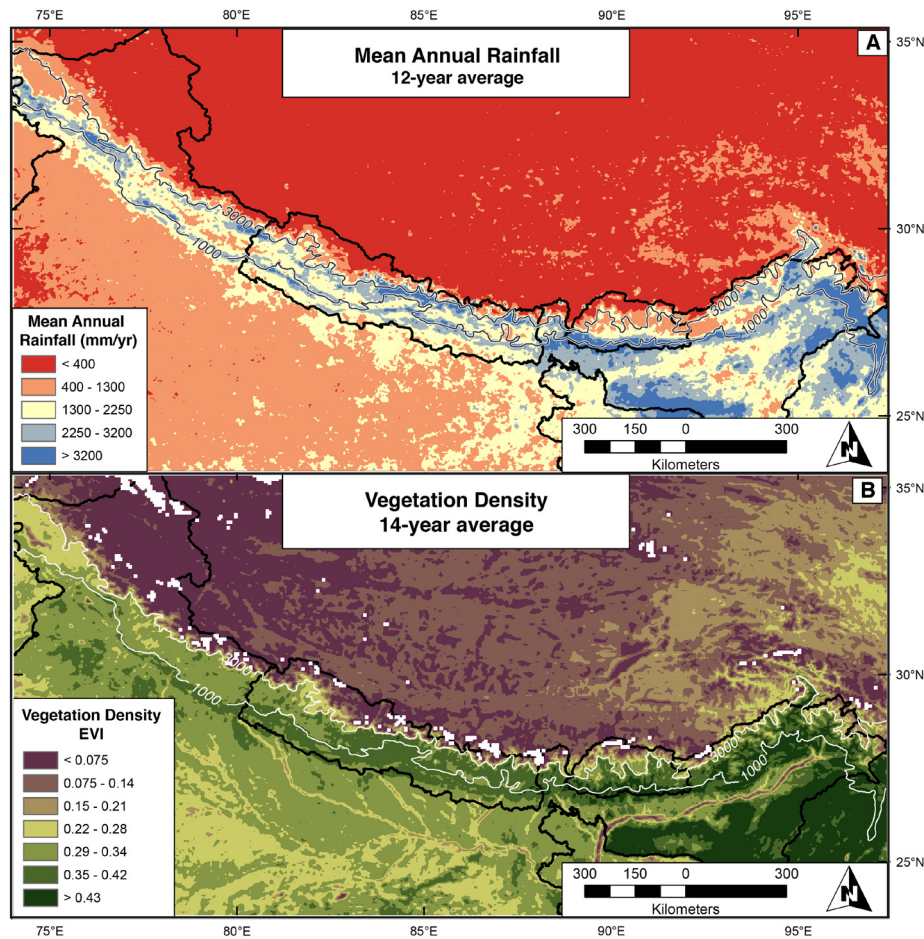


**Fig. 1.** Regional distribution of mean annual rainfall (A) and vegetation density (B) of the Himalayan region. Mean annual rainfall (MAR) is from the Tropical Rainfall Measuring Mission (TRMM) calibrated 12-yr average product 2B31 (Bookhagen and Burbank, 2010). Bands of high rainfall are focused along the orographic barriers of the Lesser and Higher Himalaya, corresponding approximately to the 1000 m asl and 3000 m asl contours shown in grey. Mean annual vegetation density is characterized by the Enhanced Vegetation Index (EVI), derived from MODIS product MOD13C1 (Huete et al., 1994) and averaged over 14 yrs. Low EVI values represent sparse or bare vegetation, while high values represent dense vegetation cover. 1000 m asl and 3000 m asl contours are shown for reference in white. White areas indicate no-data regions that are snow covered. Summer and winter EVI maps can be found in Fig. S1. Black lines indicate political boundaries in both maps.

and topography complicates potential strike-perpendicular comparisons of these highly dynamic variables. Nonetheless, samples for the determination of centennial to millennial denudation rates from terrestrial cosmogenic nuclides or million-year long-term erosion rates from thermochronology are mostly collected in transects perpendicular to strike of the most important structures and topographic relief. One way to minimize these complications is to consider a broader region characterized by an along-strike climatic gradient. In the Himalaya, mean annual rainfall (MAR) decreases as the moisture-bearing winds of the ISM travel westward from their primary moisture source in the Bay of Bengal (e.g., Barros et al., 2006). The east to west rainfall gradient (Fig. 1A) corresponds to an along-strike decrease in vegetation density (Fig. 1B). We take advantage of these along-strike gradients, 12 new  $^{10}\text{Be}$  terrestrial cosmogenic nuclide (TCN) denudation rates and previously published denudation rates from the Himalaya (Godard et al., 2014; Scherler et al., 2014; Le Roux-Mallouf et al., 2015; Morell et al., 2015; Olen et al., 2015; Portenga et al., 2015) to investigate the relationships between climate, denudation rates, and topography along strike of the Himalaya. We assess the potential influence of rainfall and vegetation using 12 yrs of calibrated remotely-sensed rainfall (TRMM 2B31, Bookhagen and Burbank, 2010) and 14 yrs of remotely-sensed vegetation density measurements (MODIS MOD13C1, Huete et al., 1994). We combine this analysis with topographic metrics, lithologic and tectonic constraints, and the compiled dataset of  $^{10}\text{Be}$  TCN denuda-

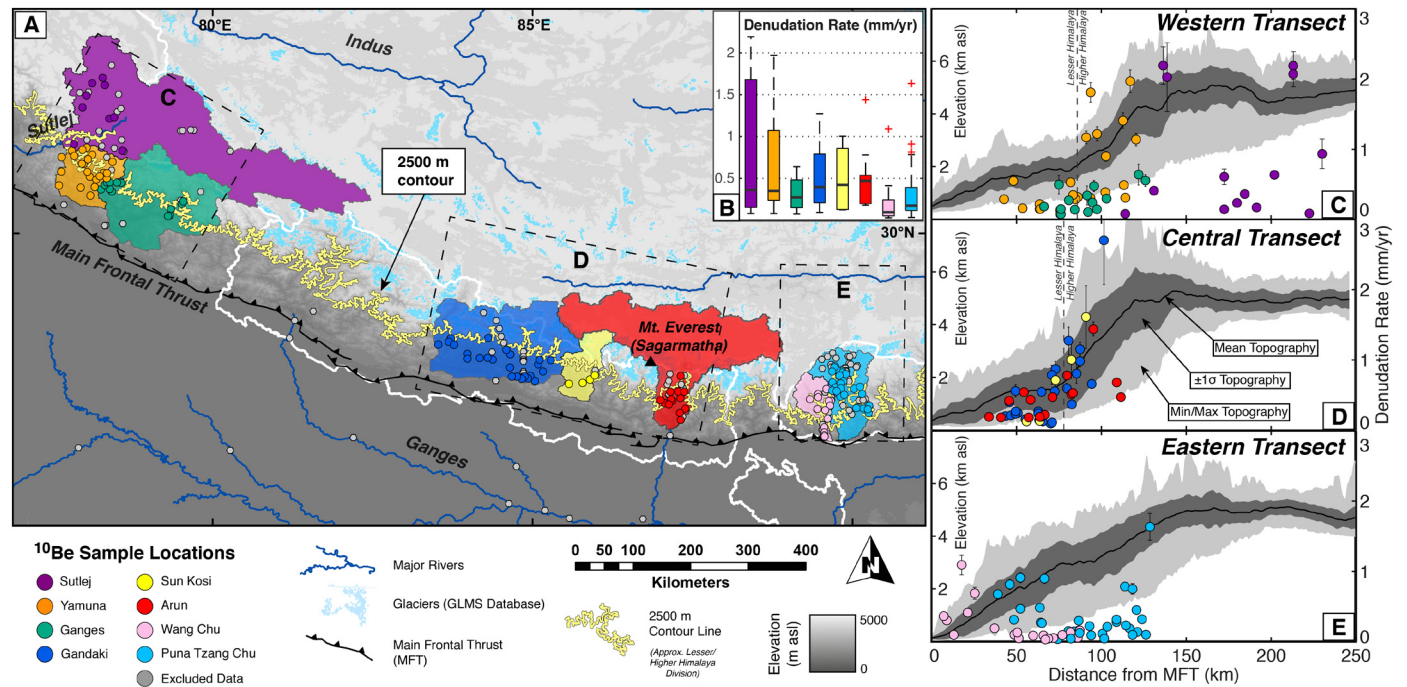
tion rates. Several studies have highlighted the dominance of tectonic uplift in forcing denudation rates across strike of the Himalaya (e.g., Burbank et al., 2003; Godard et al., 2014; Scherler et al., 2014). In this study, however, we document evidence that along-strike of the Himalaya, climate and vegetation influence both the variability of denudation rates around long-term means, and the functional relationship between denudation rates and topography.

## 2. Synthesis and new observations: denudation rates across the Himalaya

To characterize denudation rates along strike of the Himalaya, we compiled a dataset of 195  $^{10}\text{Be}$  TCN denudation rates from recently published studies (Table S1). The compiled dataset was divided into major catchment; from west to east, they are: the Sutlej (Table 1), Yamuna (Scherler et al., 2014), Upper Ganges (Morell et al., 2015), Gandaki (Godard et al., 2014), Sun Kosi (Godard et al., 2014), Arun (Olen et al., 2015), Wang Chu (Le Roux-Mallouf et al., 2015), and Puna Tzang Chu (Le Roux-Mallouf et al., 2015; Portenga et al., 2015) (Fig. 2A). All denudation rates were recalculated using the Lal/Stone scaling scheme, which takes into account time-dependent muogenic production and non-dipole geomagnetic effects (Balco et al., 2008 and references therein), and the revised  $^{10}\text{Be}$  half-life of  $1.387 \pm 0.016$  Myr (Chmeleff et al., 2010) to ensure standardized data. We have, to the best of our ability,

**Table 1**<sup>10</sup>Be TCN denudation rates and concentrations from the Sutlej.

Sample name	Sample longitude (°) <sup>a</sup>	Sample latitude (°) <sup>a</sup>	Denudation rate (mm/yr) <sup>b</sup>	Denudation rate error (mm/yr)	<sup>10</sup> Be Conc. (atom/g) <sup>c</sup>	<sup>10</sup> Be Conc. error (atoms/g)	Topographic shielding <sup>d</sup>	Ice shielding <sup>e</sup>	Snow shielding <sup>f</sup>	Total shielding
BB29	78.18	32.10	0.61	0.11	6.96E+04	1.31E+03	0.91	1.00	0.96	0.82
BB22	78.60	31.95	0.64	0.05	4.05E+04	8.39E+02	0.95	1.00	0.98	0.88
BB21	78.19	32.12	0.09	0.01	0.00E+00	0.00E+00	0.94	1.00	0.97	0.92
BB24 <sup>h</sup>	78.05	32.25	2.19	0.20	1.53E+04	7.65E+02	0.93	1.00	0.97	0.85
BB <sup>h</sup>	78.05	32.25	2.07	0.18	1.62E+04	6.69E+02	0.93	1.00	0.97	0.85
RS-7	78.19	32.09	0.15	0.02	3.84E+05	8.92E+03	0.98	0.98	0.99	0.95
BB30	78.08	32.17	0.17	0.02	0.00E+00	0.00E+00	0.97	0.97	0.98	0.92
RS-5	78.44	31.78	0.36	0.03	1.35E+05	3.49E+03	0.96	0.97	0.98	0.92
RS-6	78.41	31.80	0.24	0.03	2.32E+05	5.44E+03	0.96	0.97	0.97	0.90
BB18	78.38	31.37	2.03	0.49	2.31E+04	7.32E+02	0.92	0.95	0.97	0.80
BB11	77.74	31.40	0.08	0.01	4.63E+05	8.68E+03	0.93	0.94	0.95	0.78
BB9	78.06	31.52	0.41	0.06	9.96E+04	1.88E+03	0.92	1.00	0.94	0.81

<sup>a</sup> Catchment outlet coordinates.<sup>b</sup> Denudation rates are calculated with a bedrock density of 2.6 g cm<sup>-3</sup> and an attenuation length for spallation of  $\lambda = 160$  g cm<sup>2</sup>.<sup>c</sup> Derived from blank-corrected AMS measurements undertaken at Lawrence Livermore National Laboratory and normalized to ICN standard (Nishiizumi et al., 2007).<sup>d</sup> Topographic shielding based on 90-m SRTM DEM following Dunne et al. (1999).<sup>e</sup> Ice shielding is based on present ice coverage from the National Snow & Ice Data Center (NSIDC) Global Land Ice Measurements from Space (GLIMS) Randolph Glacier Inventory (RGI) database (<http://www.glims.org/RGI/>).<sup>f</sup> Snow shielding is based on model output from Bookhagen and Burbank (2010).<sup>h</sup> For regression analysis, the two measurements of BB24 were averaged and used as one data point.

**Fig. 2.** Compilation of <sup>10</sup>Be terrestrial cosmogenic nuclide (TCN) denudation rates from the Himalaya. (A) Digital elevation map of Himalaya (USGS GTOPO30, nominal 1-km resolution), with major rivers (dark blue), location of the Main Frontal Thrust (black), extent of present-day glaciation (light blue) (GLIMS, 2005; <http://www.glims.org/>), and political boundaries (white). Mt. Everest/Sagarmatha is shown for spatial reference. Sample locations (catchment centroids) of <sup>10</sup>Be dataset are shown as circles within major river catchments: Sutlej (purple), Yamuna (orange), Upper Ganges (green), Gandaki (dark blue), Sun Kosi (yellow), Arun (red), Wang Chu (pink), and Puna Tzang Chu (light blue). Gray circles represent samples that were excluded from the final dataset (see Supplementary Material S1–3). The approximate division of the Lesser and Higher Himalaya is shown by the 2500 m asl contour in yellow. (B) Boxplot of denudation rates from each study area from west to east, with coloring following sample color scheme in (A). Median values for each study site are represented by the thick black bar; boxes extend from the 25th to 75th percentiles; whiskers extend to all samples not considered outliers. (C–E) Strike-perpendicular swath profiles from (C) NW India (Scherler et al., 2014; Morell et al., 2015), (D) Nepal (Godard et al., 2014; Olen et al., 2015), and (E) Bhutan (Le Roux-Mallouf et al., 2015; Portenga et al., 2015). Elevation is averaged over swaths oriented perpendicular to local strike that encompass all included sample sites, denoted in (A). Thick black line denotes mean elevation, dark gray shade  $\pm 1\sigma$ , light gray shade ranges from minimum to maximum elevation values. Sample denudation rates (circles)  $\pm 1\sigma$  (vertical error bars) are plotted against the distance of the catchment centroid from the MFT, and follow the same color scheme as (A). This color scheme will be used for Figures throughout the remainder of the manuscript. (For interpretation of the references to color in this figure legend, the reader is referred to the web version of this article.)

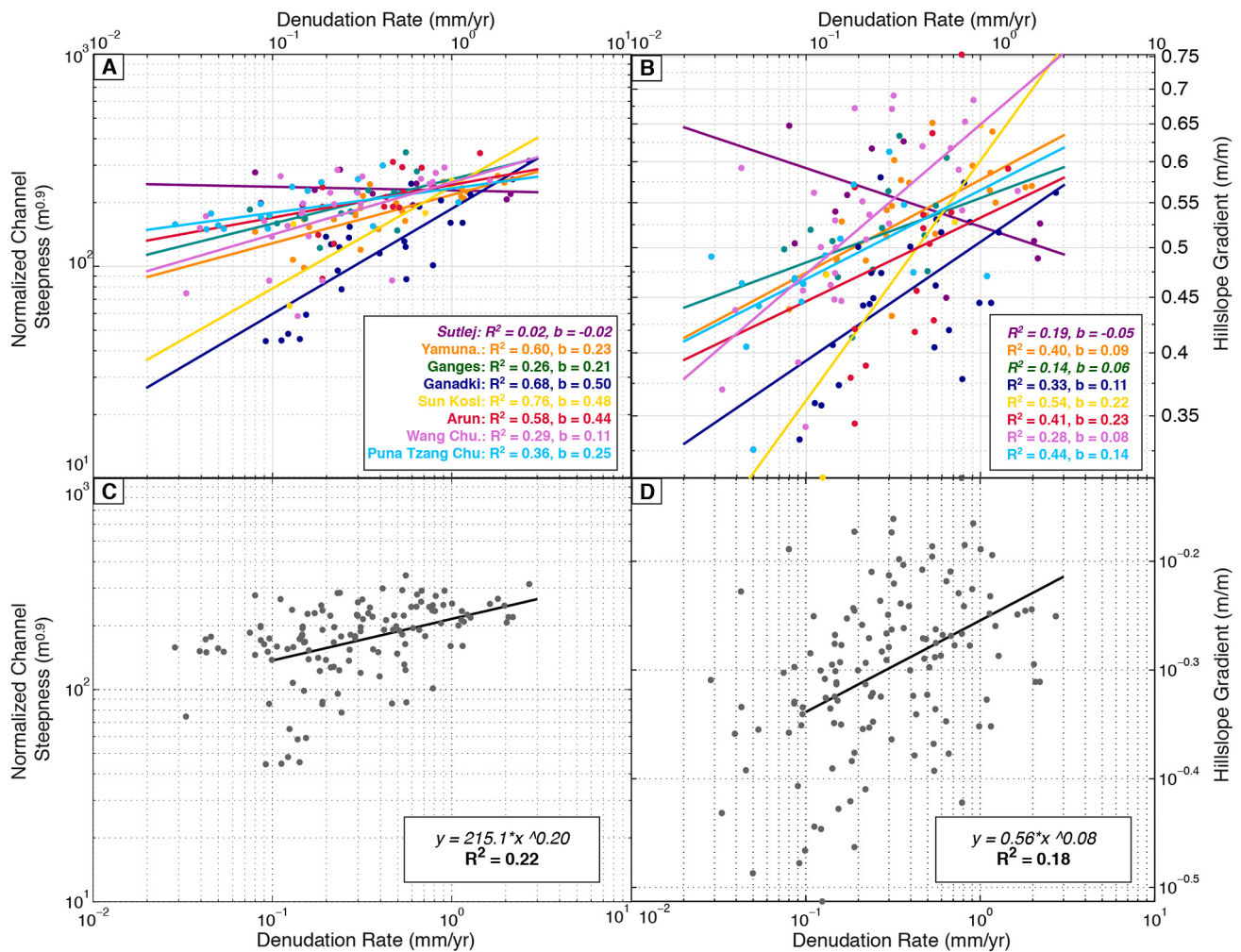


**Fig. 3.** Power-law relationship between  $^{10}\text{Be}$  TCN-derived denudation rates and catchment-mean values of (A, C) normalized channel steepness ( $k_{sn}$ ), and (B, D) hillslope gradient. (A) and (B) show data plotted with individual OLS power law regressions for each study area. Inset gives power law exponent  $b$ , following the relationship  $f(x) = ax^b$ , and goodness-of-fit ( $R^2$ ). Italic text denotes where correlation is not significant at the 95% confidence level. Additional correlation statistics for each study area can be found in Table S1. (C, D) show regression for the compiled dataset, highlighting the poor fit between denudation rates and topographic metrics when all data is considered together.

accounted for the possibility of native  $^9\text{Be}$  in the compiled dataset (see Supplementary Material S1). To avoid complications from non-fluvial and transient processes in our dataset, we excluded samples from the following environments: (1) catchments with >5% modern glacial coverage (33 samples total; 25 from Puna Tzang Chu (Portenga et al., 2015)); (2) catchments in a state of topographic transience (18 samples total; see Supplementary Material S2 for detailed description of how topographic transience was determined); (3) catchments with suspected or known recent landslide activity based on original publication (6 samples total (Scherler et al., 2014; Olen et al., 2015); see Supplementary Material S3 for further information); and (4) large trans-Himalayan catchments that integrate several climatic, tectonic, and topographic regimes (6 samples from the Arun River). After excluding transient and non-fluvial catchments, our compiled dataset contains 135 samples collected in environments dominated by fluvial erosion.

Across strike in each region, we observe that high catchment-mean denudation rates generally correspond to orographic rises, with relatively lower denudation rates where mean elevation is steady (Fig. 2C–E). Median denudation rate along strike remains relatively constant ( $0.30 \pm 0.12$  mm/yr) (Fig. 2B) over a distance of  $\sim 1500$  km, with slightly lower denudation rates in Bhutan. The range of denudation rates, however, generally decreases from west

to east, primarily by a decrease in the highest denudation rates (e.g., 75th percentile) (Fig. 2B).

A traditional approach for empirically estimating the controls of denudation rates in active orogens is to compare local (e.g., catchment-scale) denudation rates with metrics that have been shown to positively correlate with tectonic uplift, e.g., hillslope gradient, normalized channel steepness ( $k_{sn}$ ), or specific stream power (SSP) (e.g., Kirby and Whipple, 2012 and references therein). We have calculated hillslope gradient,  $k_{sn}$ , and SSP for each sampled catchment in the dataset. To account for the possibility that higher rainfall rates will induce higher erosion, we additionally calculate  $k_{sn}$  and SSP with an MAR-weighted upstream area and discharge, respectively (see Supplementary Material S4 for topographic metric calculations). In Fig. 3, we show the relationship between denudation rates and (1)  $k_{sn}$  and (2) hillslope gradient in the Himalaya. The raw data are shown with ordinary least squares (OLS) power-law regressions for each study area (Fig. 3 A, B) and for the compiled dataset (Fig. 3 C, D), following several studies that have observed a power-law relationship between topography and denudation, where  $topographic\ metric \sim (denudation\ rate)^b$  (e.g., Kirby and Whipple, 2012; Lague, 2014). In most study areas (with notable exceptions, discussed below), the power law regression provides a moderate to good fit between denudation

rates and tectonically-linked topographic metrics. However, the nature of the power law relationship varies considerably between study areas (see Table S2 for full regression results for each study area). Although denudation rates and topographic metrics are significantly correlated for the entire Himalaya dataset ( $p < 0.05$ ), the regressions provide a poor fit to the data (e.g.,  $R_{k_{sn}}^2 = 0.26$ ,  $R_{\text{Hillslope}}^2 = 0.18$ ,  $n = 135$ ) (Fig. 3C, D). The range of power-law exponents between study areas, and the poor goodness-of-fit of the compiled regression, suggests that there are one or more complicating factors causing scatter in the dataset (e.g., Kirby and Whipple, 2012). In a global compilation of  $^{10}\text{Be}$  derived catchment-mean denudation rates, Lague (2014) also found that the relationship of  $k_{sn} \sim (\text{denudation rate})^b$  varied considerably between regions, with the power-law exponent ranging from highly non-linear ( $b = 0.25$  in the Mendocino Triple Junction) to nearly linear in the Siwaliks ( $b = 0.93$ ). In the Himalaya, we likewise observe a range of power-law values characterizing the relationship between denudation rates and  $k_{sn}$ ; from highly nonlinear in the Upper Ganges and Yamuna ( $b_{k_{sn}} = 0.21\text{--}0.23$ ), to an increasingly linear relationship in the Sun Kosi and Gandaki ( $b_{k_{sn}} = 0.48\text{--}0.50$ ). In the following sections, we investigate possible causes and contributing factors to the distribution of denudation rates along strike of the Himalaya and the relationship between denudation rates and topography.

### 3. Data and methods

#### 3.1. Geology and tectonics

The Himalayan orogen can be divided into four major lithologic groups, separated by four major fault systems. From the foreland to the hinterland, they are: (1) the Cenozoic sedimentary deposits of the Siwaliks north of the Main Frontal Thrust (MFT); (2) the Lesser Himalaya Series, ranging from low- to high-grade metasediments (high-grade metasediments are also known as the Lesser Himalayan Crystalline, or LHC) north of the Main Boundary Thrust (MBT); (3) the Higher Himalayan Crystalline (HHC), predominantly granites and high-grade metamorphic rocks, separated from the LHC by the Main Central Thrust (MCT); and (4) the Paleozoic sedimentary rocks of the Tethyan Himalaya, north of the South Tibetan Detachment (STD) (e.g., Gansser, 1964). Using the geologic maps of Hodges (2000) for NW India and Nepal and Grujic et al. (2011) for Bhutan, we created a simplified lithologic map for the Himalaya divided into: Quaternary sedimentary deposits, sedimentary rocks, metasedimentary rocks, and crystalline rocks; approximately corresponding with the Siwaliks and intermontane basins, Tethyan Himalaya, Lesser Himalayan Series, and Higher Himalayan Crystalline, respectively. Based on this simplified lithologic map, we characterized each basin by the percent area in each lithology.

If lithology exerts a primary control on denudation rates or on the relationship between denudation rates and topography, we might expect basins from similar lithologies to fit the same relationship between denudation rate and topographic metric. Thus, by separating denudation rates into subsets based on basin lithology, one would expect a reduction of scatter in each subset. To test this, we binned our dataset into dominant lithology (>50% area) and performed a suite of regressions and correlation analysis between denudation rates and common tectonically-linked topographic metrics (Table 2).

The exposure of lithologic units in the Himalaya corresponds to relatively old phases of tectonic activity and mountain building during the Cenozoic (Hubbard and Harrison, 1989), and is likely not representative of tectonic activity over the last  $10^2\text{--}10^5$  yr. Thus, to investigate the link between modern denudation rates and long-term erosion rates associated with recent

**Table 2**

Parameters characterized for each catchment used in regression analysis.

Lithology and tectonics	Climate	Vegetation	Topography
% Crystalline <sup>1</sup>	TRMM 12-yr MAR (mm/yr) <sup>3</sup>	14-yr mean annual EVI <sup>6</sup>	Hillslope gradient (m/m) <sup>8</sup>
% Metasediments <sup>1</sup>	MAR-ET (mm/yr) <sup>4</sup>	Vegetation seasonality index (SI) <sup>6</sup>	$k_{sn}$ (m <sup>0.9</sup> ) <sup>9</sup>
% Sediments <sup>1</sup>	MAR-PET (mm/yr) <sup>5</sup>	Dominant land cover <sup>7</sup>	MAR-weighted $k_{sn}$ (m <sup>0.9</sup> ) <sup>9</sup>
HHC long-term erosion rate (mm/yr) <sup>2</sup>		(75th–25th percentile EVI) annual, summer <sup>6</sup>	SSP (W/m <sup>2</sup> ) <sup>10</sup> MAR-weighted SSP (W/m <sup>2</sup> ) <sup>10</sup>

<sup>1</sup> Lithologies derived from simplified map of Hodges (2000) and Grujic et al. (2011).

<sup>2</sup> Long-term erosion rates from thermochronometric inversion are from Thiede and Ehlers (2013).

<sup>3</sup> From the 12-yr mean annual rainfall product TRMM 2B31 (Bookhagen and Burbank, 2010).

<sup>4</sup> ET derived from MODIS project MOD16.

<sup>5</sup> PET derived from MODIS project MOD16.

<sup>6</sup> 14-yr average of MODIS vegetation indices MOD13C1.

<sup>7</sup> Based on the FAO Global Land Cover SHARE ([http://www.glcn.org/databases/lc\\_glcshare\\_en.jsp](http://www.glcn.org/databases/lc_glcshare_en.jsp)).

<sup>8</sup> Calculated for each pixel based on eight surrounding pixels.

<sup>9</sup> Based on stream power incision model,  $k_{sn} = (S/A)^{-0.5}$ .

<sup>10</sup> Based on the stream power incision model,  $SSP = \frac{\gamma \times Q \times S}{w}$ , where  $\gamma$  is the specific weight of water (9819 N/m<sup>3</sup>),  $Q$  is discharge (m<sup>3</sup>/s),  $S$  is the local bed slope (m/m), and  $w$  is the width of the channel (m).

tectonic activity, we compared our data to the low-temperature thermochronology dataset compiled by Thiede and Ehlers (2013). This dataset comprises Apatite fission track, Zircon fission track, and ( $^{40}\text{Ar}/^{39}\text{Ar}$ )-white mica ages and calculated erosion rates for the Higher Himalaya along strike of the orogen. Long-term erosion rates calculated from low-temperature thermochronology are averaged over 0–4 Myr and therefore represent chronologies three to four orders of magnitude longer than  $^{10}\text{Be}$ -derived denudation rates. We used the nearest measurements of long-term erosion to each major catchment to compare to TCN-derived denudation rates. In the case of data gaps, (e.g., in the Arun, see Fig. 4), we performed a bilinear interpolation between observations.

Present rates of tectonic uplift are believed to be reflected in a physiographic divide between the low-elevation and relatively low-relief Lesser Himalaya and the high-elevation, high-relief Higher Himalaya (e.g., Hodges et al., 2001; Avouac, 2003). This physiographic transition, commonly termed the PT<sub>2</sub> (Hodges et al., 2001), does not correspond strictly to the geologic boundaries of the Lesser Himalayan Series/Crystalline and the Higher Himalayan Crystalline or to the location of the MCT along strike (e.g., Hodges et al., 2001). Although there are different models for the cause of this transition, including out-of-sequence thrusting (e.g., Hodges et al., 2004) or exhumation over a mid-crustal ramp (e.g., Avouac, 2003), there is considerable data documenting differential uplift on either side of the PT<sub>2</sub>. We therefore separated our dataset into physiographic bins corresponding to: (1) the physiographic Lesser Himalaya (LH), from the MBT to the PT<sub>2</sub>; and physiographic Higher Himalaya (HH), extending from the PT<sub>2</sub> to the STD. Due to its differing tectonic and topographic setting (Le Roux-Mallouf et al., 2015) (Fig. 2e), we excluded the Bhutan data from these bins. We performed regression and correlation analysis between denudation rates and topographic and climatic metrics (Table 2) to determine if the spread of denudation rates in the compiled dataset can be explained by physiographic region and, we therefore infer, recent tectonic activity.

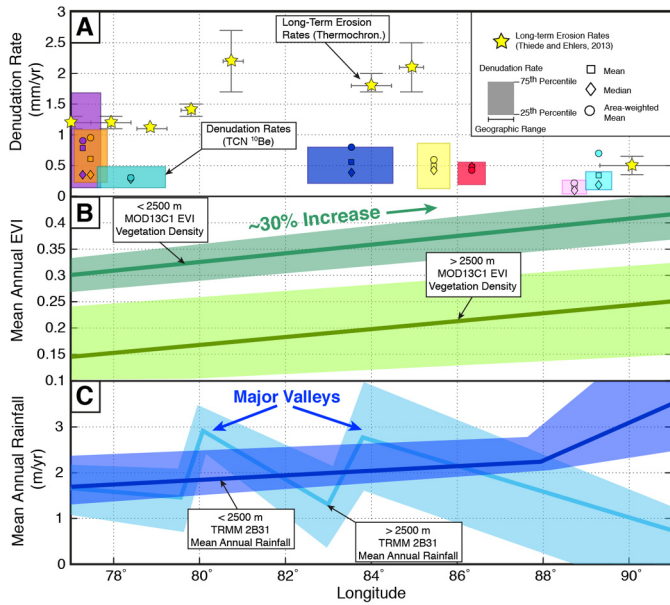


**Fig. 4.** (A) Comparison between short-term denudation rates derived from  $^{10}\text{Be}$  TCN concentrations and long-term erosion rates from low-temperature thermochronology (Thiede and Ehlers, 2013). Elevation along strike is shown in dark gray, with  $\pm 1\sigma$  in light gray. Long-term erosion rates (stars) are shown with horizontal error bars extending to the area integrated into mean long-term erosion rate values (following Thiede and Ehlers (2013); vertical error bars show  $\pm 1\sigma$  uncertainty. Short-term denudation rates are shown in boxes that extend, horizontally, to spatial extent of dataset and, vertically, to the  $\pm 1\sigma$  uncertainty. (B) Simplified vegetation density and (C) simplified mean annual rainfall along strike for the Higher and Lesser Himalaya, respectively. Swaths were taken from 1.5 decimal degree ( $\sim 110$  km) wide swaths parallel to the strike of the mountain range, centered on the Higher Himalayan front and binned by elevation, approximately corresponding to the Lesser (<2500 masl) and Higher (>2500 masl) Himalaya.

### 3.2. Climate and vegetation

Rainfall in the Himalaya was characterized using the Tropical Rainfall Measurement Mission (TRMM) 2B31 12-yr calibrated MAR, with a nominal spatial resolution of 5-km (Bookhagen and Burbank, 2010). We acknowledge that the TRMM 2B31 product does not include snowfall, which has a larger influence in the Western Himalaya, where winter precipitation is greater due to proximity to the Westerlies (e.g., Barros et al., 2006). To estimate effective water availability for surface processes, we also take into consideration the effects of evapotranspiration (ET) and potential evapotranspiration (PET). Evapotranspiration is the sum of evaporation and plant transpiration. This value is based on the Penmen–Montieth equation, which incorporates remotely-sensed atmospheric and terrestrial data, such as temperature, wind speed, relative humidity, and solar radiation (Mu et al., 2011); potential evapotranspiration is the amount of evaporation and transpiration that would occur given sufficient water. We calculated MAR-ET and MAR-PET using the MOD16 product from the Moderate-Resolution Imaging Spectroradiometer (MODIS) sensor aboard the NASA Earth Observing System Terra satellite (Mu et al., 2011).

Vegetation density in the Himalaya was quantified using the Enhanced Vegetation Index (EVI). EVI is a remotely-sensed measure of vegetation density derived from multispectral analysis of the red, near infrared, and blue wavelengths (see Supplementary Material S5 for details) (Huete et al., 1994). Valid values of EVI range from 0 to 1, with 0 representing bare land and 1 representing extremely dense vegetation cover. Due to its relatively long temporal coverage, we use the MODIS product MOD13C1, a 16-day composite EVI at 0.05 degree (nominal 5-km) resolution. Employing 14 yrs of available MODIS vegetation indices, we calculated mean annual, summer (May to October, MJJASO), and winter (November to April,

NDJFMA) EVI. To test if denudation rates are sensitive to the seasonality of vegetation density, rather than mean annual vegetation density, we calculated a seasonality index (SI) to quantify the difference between summer and winter vegetation, such that:

$$SI = \frac{EVI_{MJJASO}}{EVI_{NDJFMA}} \quad (1)$$

The seasonality index therefore quantifies how much denser summer vegetation is than winter vegetation (e.g., a value of  $SI = 1$  indicates no vegetation seasonality, while a value of  $SI = 2$  implies that vegetation is twice as dense in the summer than in the winter; see Fig. S1). The range of annual and summer EVI within each basin was measured as the difference between 75th and 25th percentiles. Assuming that higher and lower values of EVI correspond to changes in vegetative land cover type (e.g., forest, grassland, alpine vegetation), we used this range as a proxy for the variety of land cover within each basin (see Supplementary Material S5.1 for the relationship between EVI and land cover in the Himalaya). We assume that a low range of EVI within a basin corresponds to relatively uniform land cover, while a large range represents a variety of land covers within the basin. Correspondingly, we expect that when land cover is more uniform, the erosive processes acting within a basin will be more spatially uniform; when land cover varies, the erosive processes within a basin are more likely to vary.

### 3.3. Denudation rate variability and regression analysis

In the compiled dataset, we observe that the range of denudation rates generally decreases from west to east (Fig. 2B). To test possible factors controlling the variability of denudation rates along strike, we calculated the denudation rate variability for each study area as the 75th minus 25th percentile of all denudation rates within a given study area. Correlation and regression statistics ( $R^2$ ,  $R$ , and corresponding  $p$  values) were then calculated between the denudation rate variability and the median value of topographic, rainfall, and vegetation metrics for each study area (Table 2). Following several studies that suggest that the Himalaya is at steady-state over long timescales (e.g., Myr) (e.g., Lavé and Avouac, 2001), denudation rates in the orogen should reflect long-term erosion and uplift rates. Therefore, an alternative method of determining the denudation rate variability in each study area is by measuring the goodness-of-fit between measured denudation rates and tectonically-linked topographic metrics (e.g.,  $k_{sn}$ , Fig. 3A). High scatter, or a poor fit, of the data around the predicted  $k_{sn} \sim (\text{denudation rate})^b$  relationship may serve as a proxy for how denudation rates at the  $10^2$ – $10^5$  yr timescale are impacted by stochastic climatic processes. We therefore analyzed the relationship between the goodness-of-fit ( $R^2$ ) of the data to the OLS regressions presented in section 2 above as a further measure of how much each region varies from tectonically-forced long-term erosion rates.

As discussed in section 2, the functional relationships between denudation rates and topography show markedly different power-law relationships along strike. To determine what may influence the nature of this relationship, we examine the degree of linearity (power-law coefficient  $b$ ), assuming  $\text{topographic metric} \sim (\text{denudation rate})^b$ , to dominant lithologic unit, and tectonic, climatic, and vegetation metrics for each study area (Table 2). Such correlation analysis allows us to examine if, e.g., higher tectonic uplift rates result in a generally linear relationship between denudation rates and hillslope gradient. Several studies have highlighted the importance of channel geometry and width to the relationship between topography and denudation (e.g., Yanites and Tucker, 2010). We acknowledge that variations in channel width along strike may impact the relationship between topographic metrics and denudation rates (Fisher et al., 2013); however, due to lack of accurate

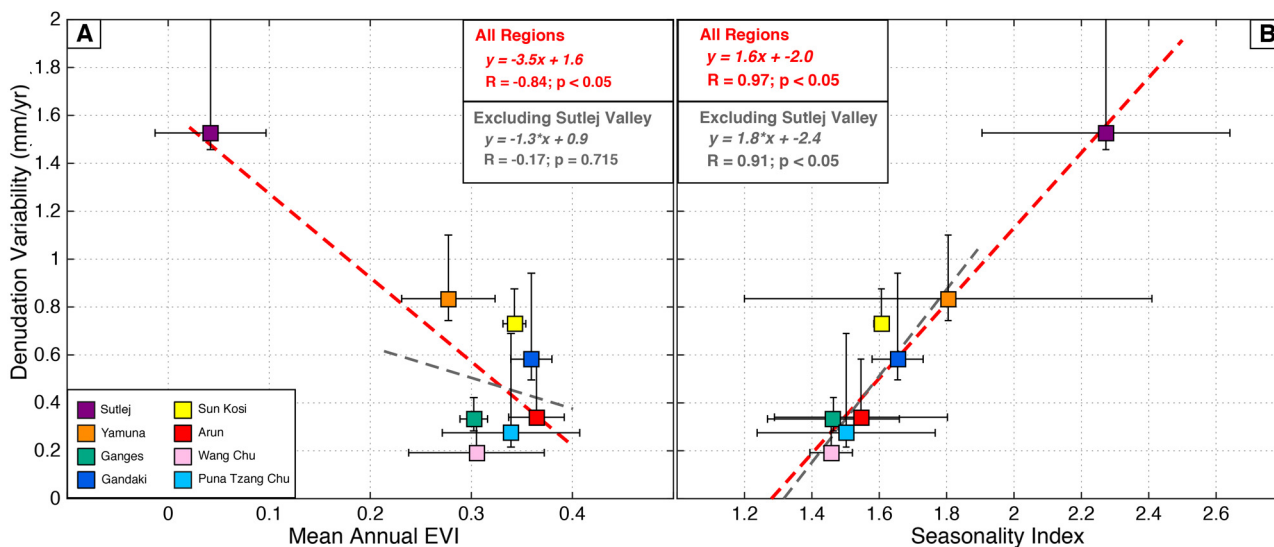


**Fig. 5.** Denudation rate variability in each study area plotted against (A) mean annual EVI  $\pm 1\sigma$ ; and (B) EVI seasonality index  $\pm 1\sigma$  (summer/winter vegetation density, cf. Equation (1)). Denudation rate variability for each study area is calculated as the 75th–25th percentile of all catchment-mean denudation rates in each study area. Vertical error bars extend to the 90th–75th percentile and 25th–10th percentile. Linear OLS regressions were performed for the entire dataset (red); and for the dataset excluding the Sutlej Valley (gray). Data points are colored by major catchment, following the color scheme in Fig. 2. Correlation and regression statistics of denudation rate variability compared to all lithologic, tectonic, and climatic parameters can be found in Table S4. (For interpretation of the references to color in this figure legend, the reader is referred to the web version of this article.)

estimates of channel width at orogen scale, we did not presently consider this factor.

## 4. Results

### 4.1. Geology and tectonics

Catchments in the compiled  $^{10}\text{Be}$  dataset are predominantly located within crystalline and metasedimentary rocks of the HHC ( $n = 44$ ) and LHC ( $n = 60$ ) units. Basins dominated by Tethyan sediments are confined to the Sutlej Valley and Bhutan (Fig. S2). We observe no basins with dominant Quaternary sedimentary fill deposits, therefore our binned subsets are: sedimentary, metasedimentary, and crystalline catchments. Denudation rates binned by lithologic units show significant correlation at the 95% confidence level with several topographic metrics, but the correlations are not consistent between lithologies, and the regression provides a poor fit to the data ( $R^2 \leq 0.45$ ), and in most cases the correlation is weak ( $|R| < 0.5$ ; Table S3).

When the data is binned by physiographic region, there are no significant correlations at the 95% confidence level between denudation rates and tectonically-linked topographic metrics (e.g.,  $k_{SN}$ ) in the Higher Himalaya along strike. In the Lesser Himalaya, there are significant correlations at the 95% confidence level between denudation rates and tectonically-linked topographic metrics (e.g.,  $k_{SN}$ ); however, the correlation is weak and provides a poor fit to the regressions ( $|R| < 0.5$ ,  $R^2 \leq 0.30$  for all metrics; Table S4).

### 4.2. Climate and vegetation

In general, rainfall and vegetation density increase from west to east along the strike of the Himalaya (Fig. 4). At lower elevations ( $<2500$  masl), vegetation density and rainfall increase relatively steadily from west to east. At high elevations, however, rainfall no longer follows a clear along-strike gradient and is instead influenced by large valleys that are oriented approximately perpendicular to strike, funneling moisture into the orogen (Anders et al., 2006) (Fig. 4C). Vegetation density continues to in-

crease eastward at higher elevation, but the gradient is more subdued.

We performed correlation analysis between the entire  $^{10}\text{Be}$  dataset, as well as the HH and LH subsets, and climatic and vegetation metrics from each sample basin. Denudation rates from the entire dataset, and from the Higher Himalaya in particular, show a significant positive correlation with the range of summer EVI values in each catchment (entire dataset:  $R = 0.67$ ,  $p < 0.05$ ,  $n = 135$ ; Higher Himalaya:  $R = 0.70$ ,  $p < 0.05$ ,  $n = 29$ ). A similar, though slightly weaker, correlation exists between denudation rates and annual EVI range. We do not see the same correlation in the Lesser Himalaya, where the range of EVI (summer or annual) is relatively small (Table S4).

### 4.3. Denudation-rate variability

Denudation-rate variability in each study area shows a strong correlation with all vegetation-density metrics (Tables S5, S6). The strongest correlation is with the seasonality index, with denudation rate variability increasing as vegetation seasonality increases ( $R = 0.95$ ,  $p < 0.05$ ) (Fig. 5). There is also a strong negative correlation between denudation rate variability and vegetation density ( $R = -0.84$ ,  $p < 0.05$ ), where denudation-rate variability decreases as mean annual vegetation density increases (Fig. 5). Notably, there are no significant correlations between denudation rate variability and topographic, tectonic, lithologic, or rainfall metrics (cf. Table S6). Denudation rate variability is significantly higher in the Sutlej, where vegetation density and rainfall are considerably lower, and seasonality higher, than in the rest of the areas covered by our dataset. Therefore, to test whether or not the relationship between denudation-rate variability and vegetation holds without this outlying data point, we performed regressions excluding the Sutlej. Without the Sutlej data, the relationship between mean annual EVI and denudation rate variability breaks down ( $R = 0.13$ ,  $p > 0.1$ ) (Fig. 5A). However, seasonality remains highly correlated to denudation-rate variability even when the Sutlej data is excluded ( $R = 0.88$ ,  $p < 0.05$ ) (Fig. 5B). The regression excluding the Sutlej is nearly identical to the regression of all study areas. Measuring denudation-rate variability with the goodness-of-fit of de-

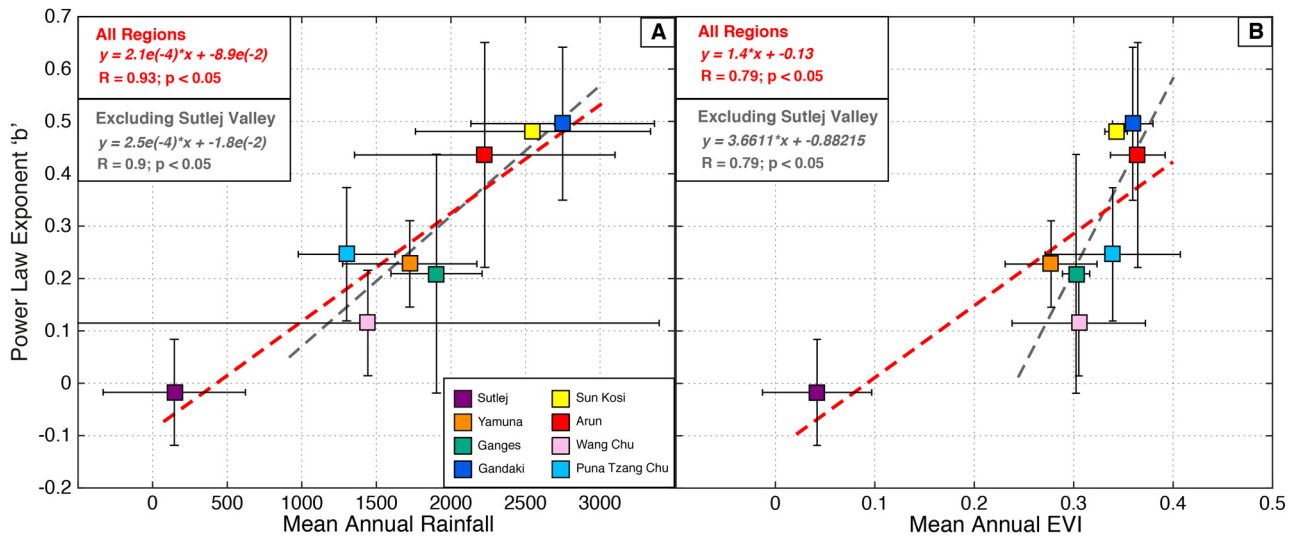


**Fig. 6.** The power-law exponent  $b$  of the functional relationship (*topographic metric*)  $\sim$  (*denudation rate*) <sup>$b$</sup>  plotted against (A) mean annual rainfall  $\pm 1\sigma$  and (B) mean annual EVI  $\pm 1\sigma$  for each study area. Vertical error bars extend to the 95% confidence intervals of  $b$ . Linear OLS regressions were performed for the entire dataset (red) and for the dataset excluding the more interior Sutlej Valley (gray). Data points are colored by major catchment, following the color scheme in Fig. 2. Correlation and regression statistics of power law exponent  $b$  to all lithologic, tectonic, and climatic parameters can be found in Table S6. (For interpretation of the references to color in this figure legend, the reader is referred to the web version of this article.)

denudation rates to the functional relationship between denudation rates and tectonically-linked  $k_{sn}$ , we observe a significant positive correlation to MAR and EVI ( $R = 0.88$ ,  $R = 0.75$  respectively) and no significant correlation to tectonic or lithologic parameters. See Table S7 for full correlation analysis.

#### 4.4. Regression analyses

We observe significant positive correlations between the power-law exponent  $b$  of the functional relationship between denudation rates and hillslope gradient,  $k_{sn}$ , and SSP and both MAR and EVI ( $R > 0.75$  in all cases; Table S8). Thus, as rainfall or vegetation density increase, the relationship between denudation rates and topographic metrics becomes increasingly linear. Conversely, when rainfall or vegetation density is low, the relationship between denudation rates and topographic metrics is increasingly non-linear. Fig. 6 shows the correlation between  $b_{k_{sn}}$  and both MAR and EVI ( $R = 0.93$ ,  $0.79$  respectively,  $p < 0.05$ ). The correlation between the power-law exponent  $b_{k_{sn}}$  and both MAR and EVI remains when the Sutlej is excluded from the analysis ( $R = 0.9$ ,  $0.79$  respectively without Sutlej data). See Table S8 for complete correlation results.

## 5. Discussion

Several studies have put forth evidence that tectonic processes control the rates and patterns of denudation across strike in the Himalaya (Hodges et al., 2001, 2004; Burbank et al., 2003; Scherler et al., 2014; Godard et al., 2014; Morell et al., 2015; Le Roux-Mallouf et al., 2015). Conversely, other recent studies argue for an along-strike climatic impact in the evolution of the Himalayan fold-and-thrust belt (Hirschmiller et al., 2014). In our analysis, we observe along-strike variations in the local variability of denudation rates and in the linearity of the functional relationship between denudation rates and topography, but find no clear evidence that tectonic uplift or lithology control these variations in modern denudation rates along strike of the orogen. No consistently significant correlation is observed between denudation rates and common, tectonically-linked topographic metrics when samples are binned by physiographic region, assumed to correspond to modern and recent tectonic uplift, or by major lithologic unit (%HHC, %LHC). Similarly, when we compare the exponent  $b$  of the

power law relationship between denudation rates and hillslope gradient, SSP, and MAR-weighted  $k_{sn}$ , we find no correlation between  $b$  and dominant lithologic unit or long-term erosion rates from the Higher Himalaya. We therefore interpret that the along-strike patterns we observe in denudation-rate variability and the linearity of the functional relationship between topographic metrics and denudation rates cannot be best explained by variations in the degree of tectonic activity or lithology along strike. Accordingly, we infer that one or more other factors must be responsible for the along-strike variations in denudation-rate variability and the relationship between denudation rates and topographic metrics.

Vegetation density (EVI) and seasonality show a strong correlation with denudation rate variability ( $R = -0.84$ ,  $0.95$ ,  $p < 0.05$ , respectively). Denudation rate variability decreases linearly as vegetation density increases, and increases as seasonality increases (Fig. 5). The link between denudation-rate variability and climate is reinforced by the positive correlation between both MAR and EVI and the goodness-of-fit of the measured denudation rates to functional relationship to the tectonically-linked  $k_{sn}$  ( $R = 0.89$ ,  $0.75$ ,  $p < 0.05$ , respectively; Table S7). The goodness-of-fit statistic approximates how well  $10^2$ – $10^5$  yr denudation rates reflect longer-term tectonically-driven erosion rates; hence as MAR and EVI increase, TCN-derived denudation rates are more likely to reflect long-term denudation rates. Lack of stabilizing vegetation cover may lead to environments that are more susceptible to stochastic climatic processes (e.g., storms) on centennial to millennial timescales, thus resulting in poor correlation of denudation rates to topographic steepness metrics (e.g.,  $k_{sn}$ , hillslope gradient). In wetter, more densely vegetated environments of the Himalaya, however, dense vegetation cover may act to buffer stochastic climatic processes and thus result in TCN-derived denudation rates that better reflect long-term, tectonically-influenced denudation rates rather than stochastic climatic processes.

The strong correlation between an increase in denudation-rate variability as the seasonality of vegetation increases suggests that not only is the mean annual vegetation density important in stabilizing erosive regimes and decreasing denudation rate variability, but that the degree of seasonal change in vegetation density also plays an important role. High seasonality results in dynamic and temporally variable vegetation density, marked by annual transi-



tions from sparse or bare winter cover to denser summer vegetation. We also measure spatially variable vegetation density by the range of EVI values within a catchment. The positive correlation we observe between denudation rates and basin EVI range suggests that the spatial variability of vegetation also directly impacts denudation rates. Studies in other regions have suggested that transitional vegetation regimes correspond to high denudation rates in the Central Andes of Chile (Carretier et al., 2013) and in the Kenyan Rift (Torres Acosta et al., 2015). Seasonality and EVI range may have a similar effect, with the highest denudation rates corresponding to regions where transitional vegetation regimes bridge the gap between temporally and spatially variable vegetation density and land cover. The link between vegetation density, seasonality, and denudation-rate variability may also be applicable when interpreting the results of paleo-denudation rates (e.g., from fluvial terraces). Significant scatter observed in paleo-denudation rates from past glacial periods, e.g., Late Pleistocene in the Garhwal Himalaya (Scherler et al., 2015), may be the result of more variable denudation during periods with sparser and more seasonal vegetation cover. Consequently, potential environmental changes, such as past increases or decreases in vegetation density, will need to be taken into account when interpreting paleo-denudation rates.

There is a positive correlation between the power-law exponent  $b$  of the functional relationship *topographic metric*  $\sim$  (*denudation rate*) <sup>$b$</sup>  and both EVI and MAR. Thus as rainfall rate or vegetation density increases, there is a corresponding increase in the linearity of the relationship between denudation rate and topographic metrics. For example, in the Gandaki, where rainfall and vegetation density is high, the relationship between denudation rate and  $k_{sn}$  is more linear ( $b_{ksn} = 0.50$ ) than in the Upper Ganges ( $b_{ksn} = 0.21$ ) or Yamuna ( $b_{ksn} = 0.23$ ), where rainfall rate and vegetation density are lower (Fig. 6, Table S8). It is notable that in the wet and densely vegetated Siwaliks, Lague (2014) found a highly linear relationship between denudation rate and  $k_{sn}$  ( $b = 0.93$ ) (Lague, 2014), supporting our observation that increasing linearity correlates with greater vegetation density and higher rainfall.

Torres Acosta et al. (2015) document a similar phenomenon in the East African Rift System. In this tectonically and climatically very different region, where denudation rates and uplift rates are slow and topographic steepness is low, the observed relationship between denudation rate and hillslope gradient is linear. However, these authors found that the slope of the relationship between denudation rate and hillslope gradient (where hillslope is the dependent variable) steepens as vegetation density increases. Thus on the steep and densely vegetated slopes of the rift escarpments, denudation rates are lower than in regions where vegetation is considerably sparser. Both the increasing linearity of largely non-linear functional relationships in the tectonically very active Himalaya and the increasing slope of the linear functional relationships in the tectonically less active East African Rift suggest that denser vegetation cover allows landscapes to become increasingly steep as a function of denudation rate, confirming the results of modeling studies (Collins et al., 2004). The shift in linearity in the relationship between denudation rates and topographic steepness can also reflect a change in the relative importance of topographic threshold values as denudation rates increase. Several studies have found that topography will steepen in response to increasing denudation rates until it reaches a threshold value, above which the landscape cannot continue to steepen in response to changes in uplift or denudation rates (e.g., Burbank et al., 1996; Montgomery, 2001). As denudation rates increase in densely vegetated regions, however, topography is able to continue to steepen to a greater degree than in sparsely vegetated regions, where threshold hillslope angles are reached earlier as denudation rates increase. A positive relationship between vegetation cover and topographic steepness has been observed in other orogens; in the

Central Andes, for example, Jeffery et al. (2014) observed that hillslope gradients positively correlate to vegetation cover, and that more continuously vegetated slopes tend to be steeper than gentler hillslopes with bare or patchy vegetation cover. Hillslope gradient and channel steepness are nonlinearly related, such that  $k_{sn} \sim (\text{hillslope gradient})^n$ , where  $n > 1$  and nonlinearity is driven by the threshold hillslope value (e.g.,  $\sim 30^\circ$ ). Bookhagen and Strecker (Bookhagen and Strecker, 2012) document a shift in the relationship between channel steepness and hillslope gradient in the Central Andes corresponding to shifts from arid, transitional, to humid environments. We propose that as vegetation density increases and threshold hillslope values correspondingly increase, channel steepness will increase more gradually with respect to hillslope gradient and denudation rates, resulting in a more linear relationship between normalized channel steepness and denudation rates (cf. Fig. 6).

The observation that the highest measured denudation rates and the highest denudation-rate variability are associated with regions characterized by the lowest rainfall rates (e.g., in the Sutlej) to provide surface runoff for erosion appears at first counterintuitive. If rainfall sets the along-strike pattern of denudation rates, the highest denudation rates should correspond to high rainfall rates. However, mean annual rainfall may not be characteristic of how rainfall impacts denudation rates. The temporal variation of rainfall (i.e., seasonality of rainfall) has been hypothesized to modulate erosion (e.g., Lague et al., 2005). Storminess has also been proposed as an important driver for erosion and sediment transport (e.g., Tucker, 2004; Wulf et al., 2012). We analyzed the seasonality of Himalayan rainfall and the number of extreme rainfall events (Fig. 7). The percent of annual rainfall that occurs during the summer (MJJASO) increases from west to east, from 40 to 80% in the western Himalaya to  $>80\%$  in the central Himalaya and Bhutan (Fig. 7A). This decrease in the seasonality of rainfall along strike is caused by the greater impact of moisture from the Winter Westerlies in the western Himalaya (e.g., Barros et al., 2006), resulting in higher winter rainfall in the western Himalaya with respect to the monsoon-dominated regions to the east. Extreme rainfall events are defined as rainfall events that exceeded the 90th percentile rainfall rate for the 12-yr time series of TRMM data at that pixel (number/year) (cf. Bookhagen, 2010). The highest number of extreme rainfall events is documented in the eastern syntaxis of the orogen in NE India and decreases steadily westward (Fig. 7B). Higher seasonality of rainfall or an increased number of storms and extreme rainfall events may drive higher and more variable denudation rates, even when mean annual rainfall is low (Snyder et al., 2003). However, we observe that denudation-rate variability is lowest in the Central Himalaya where rainfall seasonality is high ( $>80\%$ ) and extreme rainfall events are relatively frequent (3–9/yr). We argue that this effect is due to the stabilizing influence of vegetation on the landscape.

We suggest that in humid, monsoon-influenced regions with high vegetation density, vegetation density moderates the effects of highly seasonal rainfall and the impact of extreme rainfall events, resulting in denudation rates that are less impacted by stochastic climatic processes, such as large storm events, and are therefore less variable. The dense, persistent vegetation cover in these regions buffers the landscape from rainfall-driven erosion via the stabilizing effect of root cohesion, higher infiltration rates, and shielding from rain splash (e.g., Prosser and Dietrich, 1995; Gysels and Poesen, 2003; Dunne et al., 2010). Where vegetation density is low, rainfall converts rapidly into surface runoff to drive erosion. The western regions of the Himalaya (e.g., Sutlej, Yamuna) simultaneously display high vegetation seasonality and relatively low rainfall seasonality. Persistent winter rainfall, rare in Nepal and Bhutan, therefore has the potential to cause a greater impact on the landscape when vegetation density is especially low.

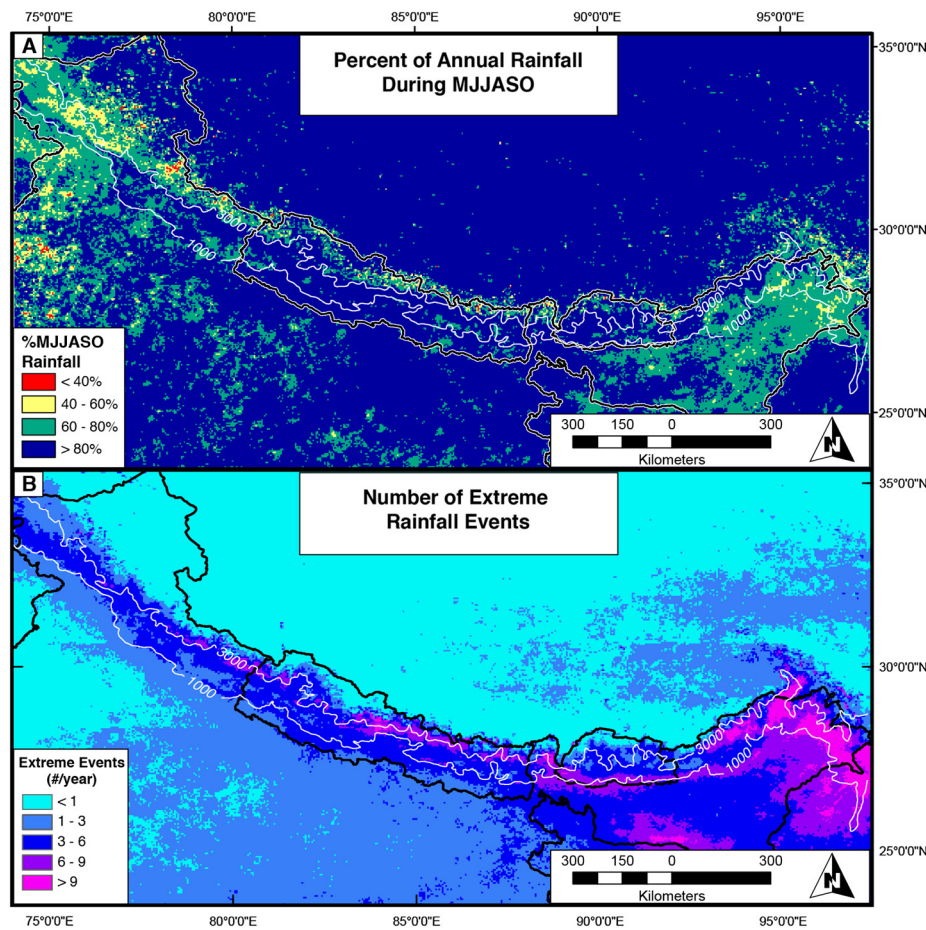


**Fig. 7.** (A) Map of TRMM2B31 rainfall seasonality for the Himalaya region. Rainfall seasonality is defined as the percent of total annual rainfall that occurs during the MJJASO summer months (Bookhagen and Burbank, 2010). (B) Map of extreme rainfall events for the Himalaya region. Extreme events are defined as those above the 90th percentile of the 12-yr time series for each pixel.

Although the number of extreme events is typically lower in the NW Himalaya, storms that do occur, or that penetrate far into the region, can have a larger impact. Without the stabilizing effect of dense vegetation cover, rainfall in these sparsely vegetated regions is able to mobilize and evacuate significantly more sediment (Wulf et al., 2012) than in more vegetated regions. This results in highly variable denudation rates that are likely driven on centennial timescales by stochastic climatic events rather than reflecting tectonic uplift rates.

## 6. Conclusions

Our study of denudation rate measurements from fluvial catchments along strike of the Himalayan orogen highlights the importance of climate and vegetation in influencing both the rates and variability of denudation. We observe a strong link between the pattern of denudation rates and climatic factors, such as rainfall and vegetation density, along strike. Importantly, denudation-rate variability is strongly correlated to vegetation density ( $R = -0.84$ ,  $p < 0.05$ ) and the vegetation seasonality ( $R = 0.95$ ,  $p < 0.05$ ). We argue that along strike of the Himalaya, vegetation density buffers the stochastic climatic processes that cause greater variability on centennial timescales around longer-timescale, tectonically-driven mean erosion and uplift rates. Such that in more densely vegetated environments, denudation rates measured with  $^{10}\text{Be}$  TCN are less variable and more indicative of tectonic rates of uplift and erosion. Furthermore, vegetation density and mean annual rainfall modulate the relationship between denudation rates and topography in a highly active and dynamic orogen. The degree of linearity

between denudation rate and topographic metrics (e.g., hillslope gradient, SSP,  $k_{SN}$ ) increases as mean annual rainfall and vegetation density increase. The result is a more linear response of topography and topographic steepness to changes in denudation rates in wet, densely vegetated environments, as opposed to a highly non-linear response in dry, sparsely vegetated environments. Overall, our study highlights the importance of vegetation in understanding the relationship between denudation rates and regional climate and tectonics, even in a tectonically active and highly dynamic orogen such as the Himalaya. Further studies of how vegetation affects denudation and topography in different tectonic settings will greatly increase our understanding of how these important surface processes interact globally.

## Acknowledgements

This project was funded by HIMPAC research group (Himalayas: Modern and Past Climates), funded by German Science Foundation (DFG) STR 373/27-1 and 28-1, and the DFG graduate school GRK1364 (Project GRK 1364/2). We thank Veronica Torres Acosta and Patricia Eugster for helpful discussions. This manuscript was greatly improved by thoughtful and constructive reviews by Kelin Whipple and Douglas Burbank.

## Appendix A. Supplementary material

Supplementary material related to this article can be found online at <http://dx.doi.org/10.1016/j.epsl.2016.03.047>.

## References

- Anders, A.M., Roe, G.H., Hallet, B., Montgomery, D.R., Finnegan, N.J., Putkonen, J., 2006. Spatial patterns of precipitation and topography in the Himalaya. *Spec. Pap., Geol. Soc. Am.* 398, 39–53.
- Avouac, J.P., 2003. Mountain building, erosion, and the seismic cycle in the Nepal Himalaya. *Adv. Geophys.* 46, 1–80.
- Balco, G., Stone, J.O., Lifton, N.A., Dunai, T.J., 2008. A complete and easily accessible means of calculating surface exposure ages or erosion rates from  $^{10}\text{Be}$  and  $^{26}\text{Al}$  measurements. *Quat. Geochronol.* 3 (3), 174–195.
- Barros, A.P., Chiao, S., Lang, T.J., Burbank, D.W., Putkonen, J., 2006. From weather to climate—seasonal and interannual variability of storms and implications for erosion processes in the Himalaya. *Spec. Pap., Geol. Soc. Am.* 398, 17–38.
- Bookhagen, B., 2010. Appearance of extreme monsoonal rainfall events and their impact on erosion in the Himalaya. *Geomorphol. Nat. Hazards Risk* 1 (1), 37–50.
- Bookhagen, B., Burbank, D.W., 2010. Toward a complete Himalayan hydrological budget: spatiotemporal distribution of snowmelt and rainfall and their impact on river discharge. *J. Geophys. Res., Earth Surf.* 115 (F3), F03019.
- Bookhagen, B., Strecker, M.R., 2012. Spatiotemporal trends in erosion rates across a pronounced rainfall gradient: examples from the southern Central Andes. *Earth Planet. Sci. Lett.* 327–328 (0), 97–110.
- Burbank, D.W., Leland, J., Fielding, E., Anderson, R.S., Brozovic, N., Reid, M.R., Duncan, C., 1996. Bedrock incision, rock uplift and threshold hillslopes in the northwestern Himalayas. *Nature* 379 (8), 505–510.
- Burbank, D.W., Blythe, A.E., Putkonen, J., Pratt-Sitaula, B., Gabet, E., Oskin, M., Barros, A., Ojha, T.P., 2003. Decoupling of erosion and precipitation in the Himalayas. *Nature* 426 (6967), 652–655.
- Carretier, S., et al., 2013. Slope and climate variability control of erosion in the Andes of central Chile. *Geology* 41 (2), 195–198.
- Chmeleff, J., von Blanckenburg, F., Kossert, K., Jakob, D., 2010. Determination of the  $^{10}\text{Be}$  half-life by multicollector ICP-MS and liquid scintillation counting. *Nucl. Instrum. Methods Phys. Res., Sect. B, Beam Interact. Mater. Atoms* 268 (2), 192–199.
- Collins, D.B.G., Bras, R.L., Tucker, G.E., 2004. Modeling the effects of vegetation–erosion coupling on landscape evolution. *J. Geophys. Res., Earth Surf.* 109 (F3), F03004.
- Dietrich, W.E., Perron, J.T., 2006. The search for a topographic signature of life. *Nature* 439 (7075), 411–418.
- Dunne, J., Elmore, D., Muzikar, P., 1999. Scaling factors for the rates of production of cosmogenic nuclides for geomorphic shielding and attenuation at depth on sloped surfaces. *Geomorphology* 27 (1–2), 3–11.
- Dunne, T., Malmon, D.V., Mudd, S.M., 2010. A rain splash transport equation assimilating field and laboratory measurements. *J. Geophys. Res., Earth Surf.* 115 (F1), n/a–n/a.
- Fisher, G.B., Bookhagen, B., Amos, C.B., 2013. Channel planform geometry and slopes from freely available high-spatial resolution imagery and DEM fusion: implications for channel width scalings, erosion proxies, and fluvial signatures in tectonically active landscapes. *Geomorphology* 194 (0), 46–56.
- Gansser, A., 1964. *Geology of the Himalayas*.
- Godard, V., Bourlès, D.L., Spinabella, F., Burbank, D.W., Bookhagen, B., Fisher, G.B., Moulin, A., Lèanni, L., 2014. Dominance of tectonics over climate in Himalayan denudation. *Geology*.
- Grujic, D., Warren, C.J., Wooden, J.L., 2011. Rapid synconvergent exhumation of Miocene-aged lower orogenic crust in the eastern Himalaya. *Lithosphere* 3 (5), 346–366.
- Gyssels, G., Poesen, J., 2003. The importance of plant root characteristics in controlling concentrated flow erosion rates. *Earth Surf. Process. Landf.* 28 (4), 371–384.
- Hirschmiller, J., Grujic, D., Bookhagen, B., Coutand, I., Huyghe, P., Mugnier, J.-L., Ojha, T., 2014. What controls the growth of the Himalayan foreland fold-and-thrust belt? *Geology*.
- Hodges, K.V., 2000. Tectonics of the Himalaya and southern Tibet from two perspectives. *Geol. Soc. Am. Bull.* 112 (3), 324–350.
- Hodges, K.V., Hurtado, J., Whipple, K.X., 2001. Southward extrusion of Tibetan crust and its effect on Himalayan tectonics. *Tectonics* 20 (6), 799–809.
- Hodges, K.V., Wobus, C., Ruhl, K., Schildgen, T., Whipple, K., 2004. Quaternary deformation, river steepening, and heavy precipitation at the front of the Higher Himalayan ranges. *Earth Planet. Sci. Lett.* 220 (3–4), 379–389.
- Hubbard, M.S., Harrison, T.M., 1989.  $^{40}\text{Ar}/^{39}\text{Ar}$  age constraints on deformation and metamorphism in the main central thrust zone and Tibetan slab, eastern Nepal Himalaya. *Tectonics* 8 (4), 865–880.
- Huete, A.R., Justice, C.O., Liu, H., 1994. Development of vegetation and soil indices for MODIS-EOS. *Remote Sens. Environ.* 49 (3), 224–234.
- Istanbulluoglu, E., Bras, R.L., 2005. Vegetation-modulated landscape evolution: effects of vegetation on landscape processes, drainage density, and topography. *J. Geophys. Res., Earth Surf.* 110 (F2), F02012.
- Istanbulluoglu, E., Tarboton, D.G., Pack, R.T., Luce, C.H., 2004. Modeling of the interactions between forest vegetation, disturbances, and sediment yields. *J. Geophys. Res., Earth Surf.* 109 (F1), F01009.
- Jeffery, M.L., Yanites, B.J., Poulsen, C.J., Ehlers, T.A., 2014. Vegetation-precipitation controls on Central Andean topography. *J. Geophys. Res., Earth Surf.* 2013JF002919.
- Kirby, E., Whipple, K.X., 2012. Expression of active tectonics in erosional landscapes. *J. Struct. Geol.* 44 (0), 54–75.
- Lague, D., 2014. The stream power river incision model: evidence, theory and beyond. *Earth Surf. Process. Landf.* 39 (1), 38–61.
- Lague, D., Hovius, N., Davy, P., 2005. Discharge, discharge variability, and the bedrock channel profile. *J. Geophys. Res., Earth Surf.* 110 (F4), F04006.
- Lamb, M.P., Scheingross, J.S., Amidon, W.H., Swanson, E., Limaye, A., 2011. A model for fire-induced sediment yield by dry ravel in steep landscapes. *J. Geophys. Res., Earth Surf.* 116 (F3), n/a–n/a.
- Langbein, W., Schumm, S., 1958. Yield of sediment in relation to mean annual precipitation. *Trans. Am. Geophys. Union* 39, 1076–1084.
- Lavé, J., Avouac, J.P., 2001. Fluvial incision and tectonic uplift across the Himalayas of central Nepal. *J. Geophys. Res., Solid Earth* 106 (B11), 26561–26591.
- Le Roux-Mallouf, R., et al., 2015. Evidence for a wide and gently dipping Main Himalayan Thrust in western Bhutan. *Geophys. Res. Lett.* 42 (9), 3257–3265.
- Montgomery, D.R., 2001. Slope distributions, threshold hillslopes, and steady-state topography. *Am. J. Sci.* 301 (4–5), 432–454.
- Morell, K.D., Sandiford, M., Rajendran, C., Rajendran, K., Alimanovic, A., Fink, D., Sanwal, J., 2015. Geomorphology reveals active décollement geometry in the central Himalayan seismic gap. *Lithosphere* 7 (3), 247–256.
- Mu, Q., Zhao, M., Running, S.W., 2011. Improvements to a MODIS global terrestrial evapotranspiration algorithm. *Remote Sens. Environ.* 115 (8), 1781–1800.
- Nishiizumi, K., Imamura, M., Caffee, M.W., Southon, J.R., Finkel, R.C., McAninch, J., 2007. Absolute calibration of  $^{10}\text{Be}$  AMS standards. *Nucl. Instrum. Methods Phys. Res., Sect. B* 258 (2), 403–413.
- Olen, S.M., Bookhagen, B., Hoffmann, B., Sachse, D., Adhikari, D.P., Strecker, M.R., 2015. Understanding erosion rates in the Himalayan orogen: a case study from the Arun Valley. *J. Geophys. Res., Earth Surf.* 120 (10), 2080–2102.
- Portenga, E.W., Bierman, P.R., Duncan, C., Corbett, L.B., Kehrwald, N.M., Rood, D.H., 2015. Erosion rates of the Bhutanese Himalaya determined using in situ-produced  $^{10}\text{Be}$ . *Geomorphology* 233, 112–126.
- Prosser, I.P., Dietrich, W.E., 1995. Field experiments on erosion by overland flow and their implication for a digital terrain model of channel initiation. *Water Resour. Res.* 31 (11), 2867–2876.
- Scherler, D., Bookhagen, B., Strecker, M.R., 2014. Tectonic control on  $^{10}\text{Be}$ -derived erosion rates in the Garhwal Himalaya, India. *J. Geophys. Res., Earth Surf.* 2013JF002955.
- Scherler, D., Bookhagen, B., Wulf, H., Preusser, F., Strecker, M.R., 2015. Increased late Pleistocene erosion rates during fluvial aggradation in the Garhwal Himalaya, northern India. *Earth Planet. Sci. Lett.* 428, 255–266.
- Snyder, N.P., Whipple, K.X., Tucker, G.E., Merritts, D.J., 2003. Channel response to tectonic forcing: field analysis of stream morphology and hydrology in the Mendocino triple junction region, northern California. *Geomorphology* 53 (1–2), 97–127.
- Thiede, R.C., Ehlers, T.A., 2013. Large spatial and temporal variations in Himalayan denudation. *Earth Planet. Sci. Lett.* 371–372 (0), 278–293.
- Torres Acosta, V., Schildgen, T.F., Clarke, B.A., Scherler, D., Bookhagen, B., Wittmann, H., von Blanckenburg, F., Strecker, M.R., 2015. Effect of vegetation cover on millennial-scale landscape denudation rates in East Africa. *Lithosphere*.
- Tucker, G.E., 2004. Drainage basin sensitivity to tectonic and climatic forcing: implications of a stochastic model for the role of entrainment and erosion thresholds. *Earth Surf. Process. Landf.* 29 (2), 185–205.
- West, A., Arnold, M., Aumaitre, G., Bourlès, D., Keddadouche, K., Bickle, M., Ojha, T., 2015. High natural erosion rates are the backdrop for present-day soil erosion in the agricultural Middle Hills of Nepal.
- Wulf, H., Bookhagen, B., Scherler, D., 2012. Climatic and geologic controls on suspended sediment flux in the Sutlej River Valley, western Himalaya. *Hydrol. Earth Syst. Sci.* 16 (7), 2193–2217.
- Yanites, B.J., Tucker, G.E., 2010. Controls and limits on bedrock channel geometry. *J. Geophys. Res., Earth Surf.* 115 (F4), n/a–n/a.